


Quench dynamics of spin in quantum dots coupled to spin-polarized leads

Kacper Wrześniewski* and Ireneusz Weymann†

Faculty of Physics, Adam Mickiewicz University, ul. Uniwersytetu Poznańskiego 2, 61-614 Poznań, Poland (Received 22 March 2019; revised manuscript received 17 June 2019; published 3 July 2019)

We investigate the quench dynamics of a quantum dot strongly coupled to spin-polarized ferromagnetic leads. The real-time evolution is calculated by means of the time-dependent density-matrix numerical renormalization group method implemented within the matrix product states framework. We examine the system's response to a quench in the spin-dependent coupling strength to ferromagnetic leads as well as in the position of the dot's orbital level. The spin dynamics is analyzed by calculating the time-dependent expectation values of the quantum dot's magnetization and occupation. Based on these, we determine the time dependence of a ferromagnetic-contact-induced exchange field and predict its nonmonotonic buildup. In particular, two timescales are identified, describing the development of the exchange field and the dot's magnetization sign change. Finally, we study the effects of finite temperature on the dynamical behavior of the system.

DOI: [10.1103/PhysRevB.100.035404](https://doi.org/10.1103/PhysRevB.100.035404)**I. INTRODUCTION**

The investigations concerning dynamical properties of quantum impurity systems are of great importance for the development of nanoscale and, in general, condensed-matter physics. Precise control and manipulation of spin and charge degrees of freedom in such systems, as well as an understanding of the relevant timescales, is a necessary requirement for further applications in spintronics [1,2] or for quantum-information processing [3,4]. In addition, the analysis of dynamical behavior of various quantum impurity models provides important knowledge about the charge and spin transport through nanostructures, and sheds new light on the effects of decoherence and dissipation [5].

A quantum impurity system can be regarded as composed of a confined, zero-dimensional subsystem interacting with an infinitely large environment. A prominent example that has recently been the subject of vast theoretical and experimental explorations is a system composed of quantum dots or molecules attached to external leads. Current nanofabrication techniques allow in particular for engineering devices consisting of multiple quantum dots in various geometrical arrangements and with precisely tuned parameters. This provides an unprecedented opportunity for experimental investigations of many important effects present in such systems, including the Kondo effect [6,7], superconducting correlations and Andreev transport [8,9], quantum interference effects, as well as various charge and spin transport phenomena among many others [10–12].

In addition to examinations of the steady-state transport properties of quantum dot systems, there have been an increasing number of experiments conducted in the strong-coupling regime, where the dynamics and relaxation [13–16] as well as different quench protocols and the Kondo physics have been

investigated in a time domain [17,18]. From a theoretical point of view, the dynamical properties of low-dimensional systems have been attracting considerable attention [19–24]. However, an accurate description of the dynamics in such systems poses a considerable challenge due to electronic correlations. Recently, there have been significant advances in this regard [25–33], especially by resorting to various renormalization group schemes [34–44].

In this paper, we address the problem of dynamical behavior of quantum dots attached to spin-polarized leads, and we focus on the strong-coupling regime, when electron correlations can give rise to the Kondo effect [45,46]. Perturbative approaches fail to capture strong correlations due to infrared divergences; therefore, we turn to Wilson's numerical renormalization group (NRG) method [47]—a very accurate, nonperturbative method for calculating transport properties of quantum impurity systems, including quantum dots coupled to external leads. As we are interested in charge and spin dynamics, we use the extension of NRG introduced by Anders and Schiller, namely the time-dependent numerical renormalization group (tNRG) method [48,49]. This method was subsequently generalized by Nghiem and Costi to finite temperatures, multiple quenches, and the possibility of studying time evolution in response to general pulses and periodic driving [50–52]. While tNRG has already provided valuable insight into the dynamics of Kondo-correlated molecules and quantum dots attached to nonmagnetic leads [43,53–55], the time-dependent behavior of local observables of correlated impurities with spin-polarized contacts remains rather unexplored. The goal of this paper is to fill this gap.

Quantum dots coupled to ferromagnetic electrodes have already been extensively studied in the case of stationary-state transport properties [56–59]. In particular, the competition between Kondo correlations and ferromagnetism was shown to result in many nontrivial spin-related phenomena, such as the exchange-field-induced suppression of the Kondo correlations [60–65]. Motivated by the above advances, we analyze the time-dependent properties of a single quantum

*wrzesniewski@amu.edu.pl

†weymann@amu.edu.pl

dot strongly coupled to ferromagnetic leads subject to a quantum quench. More specifically, we consider two types of quantum quenches: the first one concerns the quench in the spin-dependent coupling strength, whereas the second type of quench is associated with a change in the dot's orbital level position. We study the time evolution of the dot's magnetization and the occupation number following the quench. Finally, we also take into consideration finite-temperature effects and analyze their impact on spin dynamics.

We show that the time evolution of the dot's magnetization and occupation strongly depends on the initial conditions of the system. In particular, for the quantum dot initially occupied by a single electron, we find a range of time where the time evolution of magnetization exhibits a nonmonotonic behavior—magnetization shows oscillations as a function of time with a sign change. The corresponding sign change is also clearly visible in the time dependence of the induced exchange field. We show that this nonmonotonic buildup is a consequence of the qualitatively different time evolution of spin-resolved occupations of the quantum dot. It turns out that while the charge dynamics is mainly governed by the coupling to the majority-spin subband of the ferromagnet, the spin dynamics is determined by the coupling to the minority-spin band. Finally, we demonstrate that all these effects can be smeared out by thermal fluctuations once the inverse of temperature becomes comparable with the timescale when the interesting physics occurs.

This paper is structured as follows. Section II consists of a Hamiltonian description of the considered system, an overview of the quench protocol, and a summary of the numerical renormalization group method used for calculations of time-dependent expectation values of local observables. In Sec. III we present the numerical results and relevant analysis for the quenches in the coupling strength and orbital level position. We also present and discuss the effects of finite temperature on dynamical behavior. Finally, the work is concluded in Sec. IV.

II. THEORETICAL FRAMEWORK

A. Hamiltonian

We consider a single-level quantum dot coupled to a spin-polarized ferromagnetic lead [56–59], as shown in Fig. 1. The system is described by the single-impurity Anderson

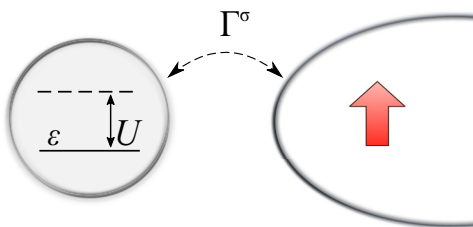


FIG. 1. Schematic of the considered system. A single-level quantum dot, with on-site energy ε and Coulomb correlations U , is attached to an effective reservoir of spin-polarized electrons with the spin-dependent coupling strength Γ^σ .

Hamiltonian, which can be generally written as

$$H = H_{\text{QD}} + H_{\text{Lead}} + H_{\text{Tun}}. \quad (1)$$

The quantum dot Hamiltonian is given by

$$H_{\text{QD}} = \varepsilon n + U n_\uparrow n_\downarrow, \quad (2)$$

where the quantum dot occupation is expressed as, $n = n_\uparrow + n_\downarrow = d_\uparrow^\dagger d_\uparrow + d_\downarrow^\dagger d_\downarrow$, with d_σ^\dagger (d_σ) being the dot's fermionic creation (annihilation) operator for an electron with spin σ and energy ε . The Coulomb correlation energy between the two electrons occupying the dot is denoted by U . The ferromagnetic lead is modeled as a reservoir of noninteracting quasiparticles,

$$H_{\text{Lead}} = \sum_{\mathbf{k}\sigma} \varepsilon_{\mathbf{k}\sigma} c_{\mathbf{k}\sigma}^\dagger c_{\mathbf{k}\sigma}, \quad (3)$$

where $c_{\mathbf{k}\sigma}^\dagger$ ($c_{\mathbf{k}\sigma}$) is the creation (annihilation) operator of an electron with momentum \mathbf{k} , spin σ , and energy $\varepsilon_{\mathbf{k}\sigma}$. Finally, the tunneling Hamiltonian reads

$$H_{\text{Tun}} = \sum_{\mathbf{k}\sigma} V_\sigma (c_{\mathbf{k}\sigma}^\dagger d_\sigma + \text{H.c.}), \quad (4)$$

where the tunnel matrix elements are denoted by V_σ and assumed to be momentum-independent. The spin-dependent coupling between the quantum dot and the lead is expressed as $\Gamma^\sigma = \pi \rho^\sigma |V_\sigma|^2$, with ρ^σ being the spin-dependent density of states of the ferromagnetic electrode. By introducing the spin polarization of the lead p , the coupling strength can be written in the following manner: $\Gamma^{\uparrow(\downarrow)} = \Gamma(1 \pm p)$, with $\Gamma^{\uparrow(\downarrow)}$ denoting the coupling to the spin-up (spin-down) electron band of the ferromagnetic lead and $\Gamma = (\Gamma^\uparrow + \Gamma^\downarrow)/2$.

It is also worth noting that the considered model is equivalent to a quantum dot coupled to the left and right leads at equilibrium with the magnetic moments of the leads forming a parallel alignment. By performing an orthogonal transformation, one can show that the quantum dot couples only to an even linear combination of the electrode's operators, with an effective coupling strength Γ and average spin polarization p [66].

B. Quench protocol

In this paper, the primary focus is on understanding the spin-resolved dynamics of the system subject to a quantum quench. In general, the time-dependent Hamiltonian describing the evolution after the quantum quench can be written as

$$H(t) = \theta(-t)H_0 + \theta(t)H, \quad (5)$$

where $\theta(t)$ is the step function. Here, the Hamiltonian H_0 is the initial Hamiltonian of the system. At time $t = 0$, the system becomes quenched, i.e., its Hamiltonian suddenly changes, and it evolves according to H . The two Hamiltonians are thus given by Eq. (1) with appropriately changed parameters. The time evolution of an expectation value of a local operator $O(t)$ can then be found from

$$O(t) \equiv \langle O(t) \rangle = \text{Tr}\{e^{-iHt} \rho_0 e^{iH_0 t} O\}, \quad (6)$$

where ρ_0 denotes the initial equilibrium density matrix of the system described by H_0 .

In the following, we study two types of quantum quenches. In the first case, the quench concerns the coupling strength Γ . It is assumed that for $t < 0$, the quantum dot is decoupled from the lead ($\Gamma_0 = 0$) and the quench takes place at $t = 0$, suddenly changing the Hamiltonian from H_0 to H , with the spin-dependent coupling to ferromagnetic contact Γ^σ being abruptly switched on. The second type of quench that we investigate involves a change in the dot's orbital level position $\varepsilon_0 \rightarrow \varepsilon$, while the coupling strength remains intact.

For those two quenches, we determine the time dependence of the expectation values of the dot's magnetization and occupation. The former can be found from

$$S_z(t) = \frac{n_\uparrow(t) - n_\downarrow(t)}{2}, \quad (7)$$

which can be easily expressed with the use of the quantum dot's operators as $n_\uparrow(t) = d_\uparrow^\dagger(t)d_\uparrow(t)$ and $n_\downarrow(t) = d_\downarrow^\dagger(t)d_\downarrow(t)$, whereas the latter is simply equal to $n(t) = n_\uparrow(t) + n_\downarrow(t)$.

C. NRG implementation

To account for various many-body effects and analyze the spin-resolved dynamics in the most accurate manner, we use Wilson's numerical renormalization group method [47,67] to find the eigenspectrum of the Hamiltonian (1). At first, the conduction band of the lead is logarithmically discretized with a discretization parameter Λ . Consequently, the discretized band is mapped on a tight-binding chain with exponentially decaying hopping between the consecutive sites, forming the Wilson chain [67]. After this transformation, the Hamiltonian (1) can be explicitly written as

$$H = H_{\text{QD}} + \sum_{\sigma} V_{\sigma} (f_{0\sigma}^{\dagger} d_{\sigma} + d_{\sigma}^{\dagger} f_{0\sigma}) + \sum_{n=0}^{\infty} \sum_{\sigma} \xi_n (f_{n\sigma}^{\dagger} f_{n+1\sigma} + f_{n+1\sigma}^{\dagger} f_{n\sigma}). \quad (8)$$

Here, the operator $f_{n\sigma}^{\dagger}$ creates an electron of spin- σ at the n th site of the Wilson chain, while ξ_n denotes the hopping integrals between the sites n and $n + 1$, respectively [47,67]. The Hamiltonian H_0 is also given by Eq. (8) with appropriately adjusted parameters.

We diagonalize both Hamiltonians, H and H_0 , using NRG [68] in N iterations and keeping up to N_K energetically lowest-lying eigenstates retained at each iteration of the NRG procedure. These states are referred to as *kept* and labeled with the superscript K . For a few first sites of the Wilson chain, $n < n_0$, all the states are kept. However, once the size of the Hilbert space exceeds N_K , which happens at a certain iteration $n = n_0$, one needs to truncate the space by discarding the high-energy eigenstates. These states are referred to as *discarded* and labeled with the superscript D . In addition, all the states of the last iteration $n = N$ are also considered as discarded states.

The discarded states $|ns\rangle^D$ at iterations $n < N$ are complemented by the state space of the rest of the chain spanned by the environmental states $|ne\rangle$ [48,49]. The resulting states

$$|nse\rangle^D \equiv |ns\rangle^D \otimes |ne\rangle \quad (9)$$

allow us to find the full many-body eigenbases

$$\sum_{nse} |nse\rangle_0^D \langle nse| = \mathbb{1} \quad \text{and} \quad \sum_{nse} |nse\rangle^D \langle nse| = \mathbb{1} \quad (10)$$

of the two Hamiltonians, H_0 and H , respectively. Here, the summation over the Wilson shells n involves only the shells where discarded states are designated, i.e., $\sum_n \equiv \sum_{n \geq n_0}$. The above eigenbases, due to the energy-scale separation, are good approximations of the eigenstates of the full NRG Hamiltonians [48,49]

$$H_0 |nse\rangle_0^X \simeq E_{0ns}^X |nse\rangle_0^X, \quad (11)$$

$$H |nse\rangle^X \simeq E_{ns}^X |nse\rangle^X, \quad (12)$$

where $X = K$ ($X = D$) denotes a kept or a discarded state.

The discarded states of the Hamiltonian H_0 are furthermore used to construct the full density matrix of the system at temperature $T \equiv 1/\beta$ [69],

$$\rho_0 = \sum_{nse} \frac{e^{-\beta E_{0ns}^D}}{Z} |nse\rangle_0^{DD} \langle nse|, \quad (13)$$

where

$$Z \equiv \sum_{nse} e^{-\beta E_{0ns}^D} \quad (14)$$

is the partition function. Note that the energies E_{0ns}^D are independent of the environmental index e . Tracing out the environmental states introduces the weight factor $w_n \equiv \frac{d^{N-n} Z_n}{Z}$ of a given iteration [69],

$$\rho_0 = \sum_n \underbrace{\frac{d^{N-n} Z_n}{Z}}_{w_n} \underbrace{\sum_s \frac{e^{-\beta E_{0ns}^D}}{Z_n} |ns\rangle_0^{DD} \langle ns|}_{\rho_{0n}}, \quad (15)$$

with

$$Z_n \equiv \sum_s e^{-\beta E_{0ns}^D} \quad (16)$$

denoting the partition function of a given iteration and d being the local dimension of the Wilson site. Consequently, the density matrix can be written in a compact form as

$$\rho_0 = \sum_n w_n \rho_{0n}. \quad (17)$$

The time-dependent expectation value $\langle O(t) \rangle$ of an operator O [cf. Eq. (6)] can be written using the complete NRG bases as

$$\langle O(t) \rangle = \sum_{nn'n''} \sum_{ss'e} \langle nse | w_{n''} \rho_{0n''} | n's'e \rangle^D \times \langle n's'e | O | nse \rangle^D e^{i(E_{ns}^D - E_{n's'}^D)t}. \quad (18)$$

Note that this formula involves a triple summation over the Wilson shells: one summation results from the definition of the full density matrix ρ_0 [cf. Eq. (17)], whereas the other two stem from the completeness relation [cf. Eq. (10)]. To make this formula computationally more efficient, such that one could make the calculations in a single-sweep fashion, we use the identity $\sum_{mn'} \equiv \sum_n^{XX' \neq KK}$, in which the double sum

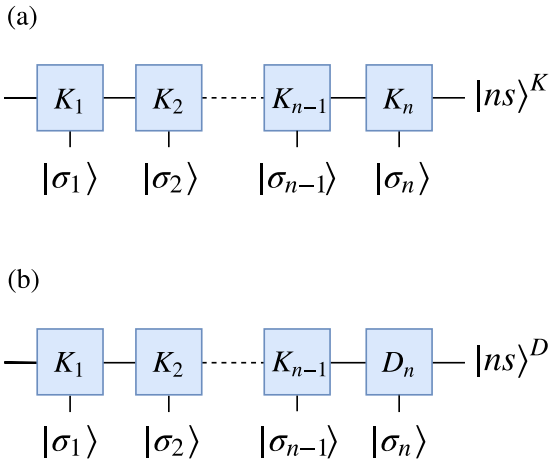


FIG. 2. Matrix product illustration of (a) kept $(|ns\rangle^K)$ and (b) discarded $(|ns\rangle^D)$ state at Wilson shell n . The bottom legs label the local states $|\sigma_n\rangle$. The blocks K_n (D_n) represent the kept (discarded) state space at Wilson shell n .

over the states of the Wilson chain is changed into a single sum over n with an additional summation over the combination of kept and discarded states, except when both states are kept [43]. Then, the formula for the expectation value, Eq. (18), becomes

$$\langle O(t) \rangle = \sum_n \sum_{n'} \sum_{ss'e}^{XX' \neq KK} X(nse|w_{n'} \rho_{0n'} |ns'e\rangle^{X'}) \times X' \langle ns'e|O|nse\rangle^X e^{i(E_{ns}^X - E_{ns'}^{X'})t}. \quad (19)$$

This formula can be directly evaluated by using NRG in the time domain [51]; however, it is more convenient to perform the time-dependent calculations in the frequency space and then apply the Fourier transformation back to the time domain [70]. The frequency-dependent expectation value $\langle O(\omega) \rangle$ of a local operator O is given by

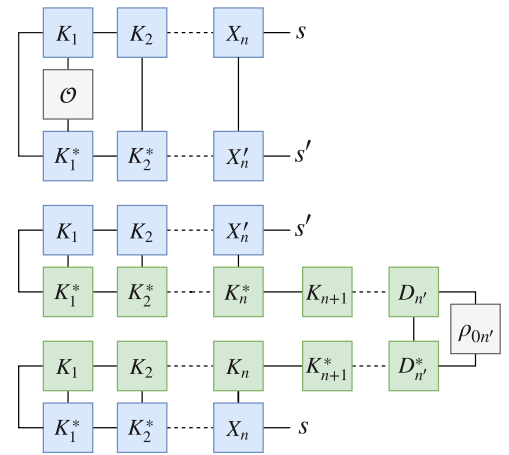
$$\langle O(\omega) \rangle = \sum_n \sum_{n'} \sum_{ss'e}^{XX' \neq KK} X(nse|w_{n'} \rho_{0n'} |ns'e\rangle^{X'}) \times X' \langle ns'e|O|nse\rangle^X \delta(\omega + E_{ns}^X - E_{ns'}^{X'}). \quad (20)$$

It is interesting to note that the calculations of the frequency-dependent expectation value can be performed in a similar fashion to the calculation of the spectral function within conventional NRG [67,69,71,72].

D. Calculation procedure

All the calculations can be conveniently performed in the matrix product states language [70,73,74]. An exemplary illustration of a kept or a discarded state $|ns\rangle^X$ is presented in Fig. 2. Using MPS diagrammatics, the frequency-dependent expectation value of an operator O given by Eq. (20) can be calculated in an iterative fashion, where the data points corresponding to $\omega = E_{ns'}^{X'} - E_{ns}^X$ are collected in appropriate energy bins on a logarithmic scale. The part of the expression for $\langle O(\omega) \rangle$ preceding the Dirac δ function can be estimated from the MPS diagrams shown in Fig. 3. In calculations, it is

(a) For $n' \geq n$



(b) For $n' < n$

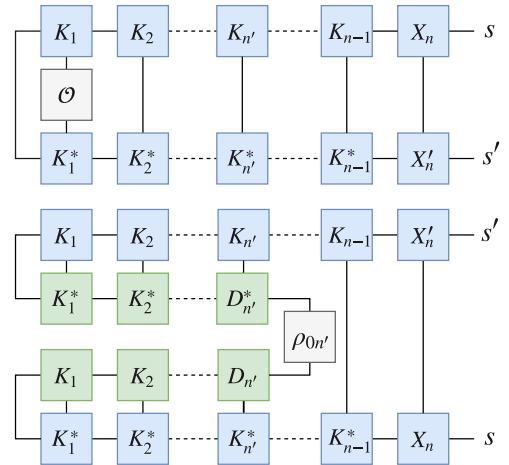


FIG. 3. Matrix product state diagrams for the calculation of a contribution to the frequency-dependent expectation value of an operator O after the quantum quench, as given by Eq. (20). The first diagram (a) shows the contribution relevant for $n' \geq n$, whereas the second diagram displayed in (b) presents the contribution for $n' < n$. These contributions need to be summed over the states s and s' and iterations n and n' . For the contribution presented in (b) there is an additional weight factor given by $d^{n'-n}$ due to the environmental states. The green squares represent the state space of the initial Hamiltonian H_0 , whereas the blue squares represent the states of the final Hamiltonian H .

important to consider separately the case of $n' \geq n$ and $n' < n$, depending on whether the density matrix ρ_0 gives the contribution at iterations equal to or larger than n or smaller than n . In the first situation, one needs to evaluate the MPS diagrams shown in Fig. 3(a). On the other hand, in the second case of $n' < n$, the corresponding diagram is illustrated in Fig. 3(b). Note that in this situation, the trace over the environmental states results in a weight factor given by $d^{n'-n}$. Notice also that at $T = 0$, i.e., for the ground state, only the first MPS diagram, which is shown in Fig. 3(a), is relevant. All these contributions need to be summed over the states and the Wilson shells,

as given explicitly in Eq. (20). Eventually, one obtains the spectral representation of an expectation value of $O(t)$ given by a sum of Dirac delta peaks with the corresponding weights O_j ,

$$O(\omega) \equiv \langle O(\omega) \rangle = \sum_j O_j \delta(\omega - \omega_j). \quad (21)$$

The delta peaks consist of one large contribution at $\omega \rightarrow 0$, which corresponds to the long-time-limit value of $O(t)$. The collected delta peaks are then log-Gaussian broadened with a broadening parameter b (except for the point at $\omega \rightarrow 0$) and Fourier-transformed back into the time domain to finally obtain

$$O(t) = \int_{-\infty}^{\infty} O(\omega) e^{-i\omega t} d\omega. \quad (22)$$

As far as NRG technicalities are concerned, in calculations we assumed the discretization parameter $\Lambda = 2$, we set the length of the Wilson chain to be $N = 80$, and we kept at least $N_K = 2000$ energetically lowest-lying eigenstates at each iteration. Moreover, to increase the accuracy of the data and suppress the band discretization effects, we employ Oliveira's z -averaging [75] by performing calculations for $N_z = 8$ different discretizations.

In Figs. 4 and 5 we show exemplary results for the quantum dot occupation number and magnetization, respectively, obtained for a quench performed in the dot's level position. The initial Hamiltonian H_0 has the orbital level set to the particle-hole symmetry point, $\varepsilon_0 = -U/2$, while for the final Hamiltonian H the level is set at resonance $\varepsilon = 0$. The collected delta peaks obtained from the calculations along with their weights, cf. Eq. (20), are shown in the top panels of Figs. 4 and 5. The black arrows at $\omega = 0$ indicate the zero-energy peak corresponding to the long-time-limit value of the corresponding expectation value. In the next step, the delta peaks are broadened using the logarithmic Gaussian kernel with the broadening parameter b [69]. The broadened data are presented in Figs. 4(b) and 5(b) for different values of the broadening parameter. It can be seen that upon increasing the value of b , the artefacts resulting from the discretization of the conduction band become damped, in a similar manner as in the approach proposed by Anders and Schiller [48,49], where a damping factor was introduced. Note, however, that the zero-frequency peak is not subject to broadening. The broadened data are subsequently Fourier-transformed to obtain the time-dependent expectation value. The time evolution of the dot's occupation number and magnetization is presented in Figs. 4(c) and 5(c), respectively, for a few selected values of b . Note that the case of $b = 0$ corresponds to obtaining $O(t)$ directly from discrete data without broadening. However, to suppress the discretization artefacts and obtain smooth data, in the next sections we use the broadening parameter equal to $b = 0.3$.

III. RESULTS AND DISCUSSION

In the following, we present and discuss the behavior of the dot's magnetization and occupation as a function of time considering quenches both in the coupling strength and the

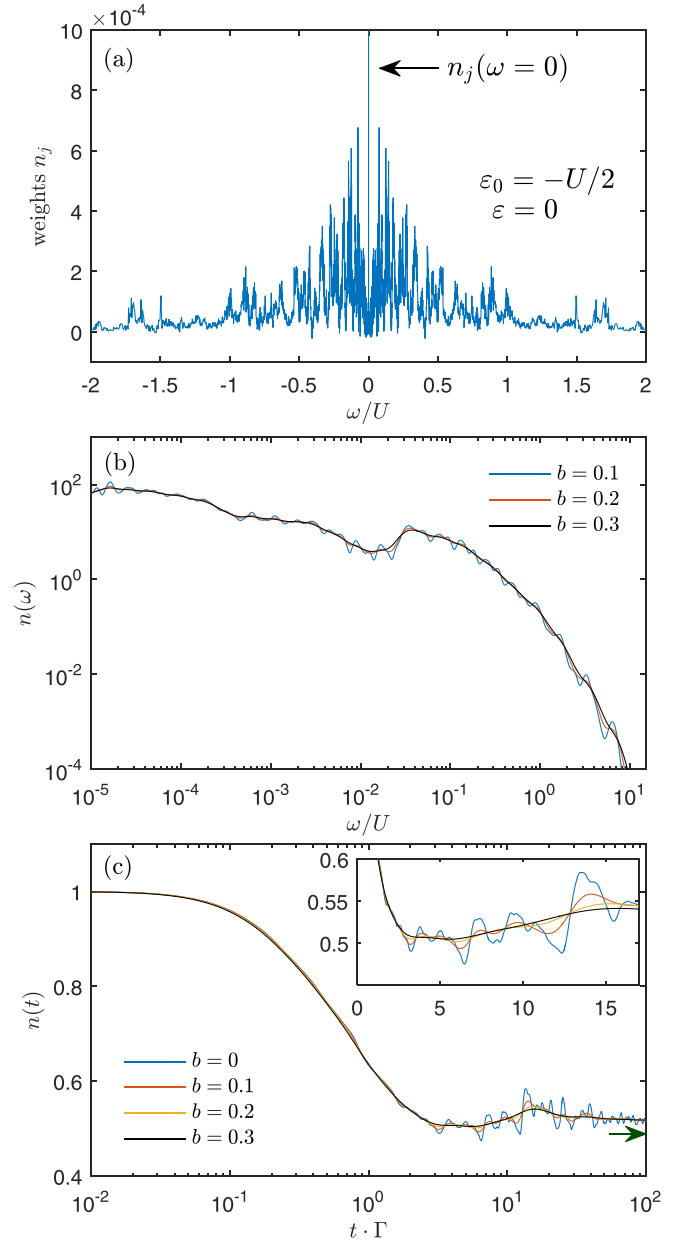


FIG. 4. The results for quench performed in the dot's level position from $\varepsilon_0 = -U/2$ to $\varepsilon = 0$. Panel (a) presents the weights n_j of collected delta peaks corresponding to the frequency-dependent local operator $n(\omega) = \sum_j n_j \delta(\omega - \omega_j)$. Panel (b) shows the absolute value of the collected δ peaks after the logarithmic-Gaussian broadening (without the point at $\omega \rightarrow 0$) for different values of the broadening parameter b , as indicated, plotted as a function of frequency ω on the logarithmic scale. The time dependence of $n(t)$ for the considered quench is shown in (c). The inset in (c) presents the dependence of $n(t)$ in the linear scale. The green arrow in (c) indicates the long-time-limit value of the dot's occupation. The parameters are $T = 0$, $U = 0.12$ (in units of band half-width), $\Gamma = U/10$, $p = 0.5$, and $\Lambda = 2$, $N_K = 2000$, $N_z = 8$.

position of the dot's orbital level. This allows us to investigate the buildup of the exchange field in the system and study its dependence on the model parameters and temperature.

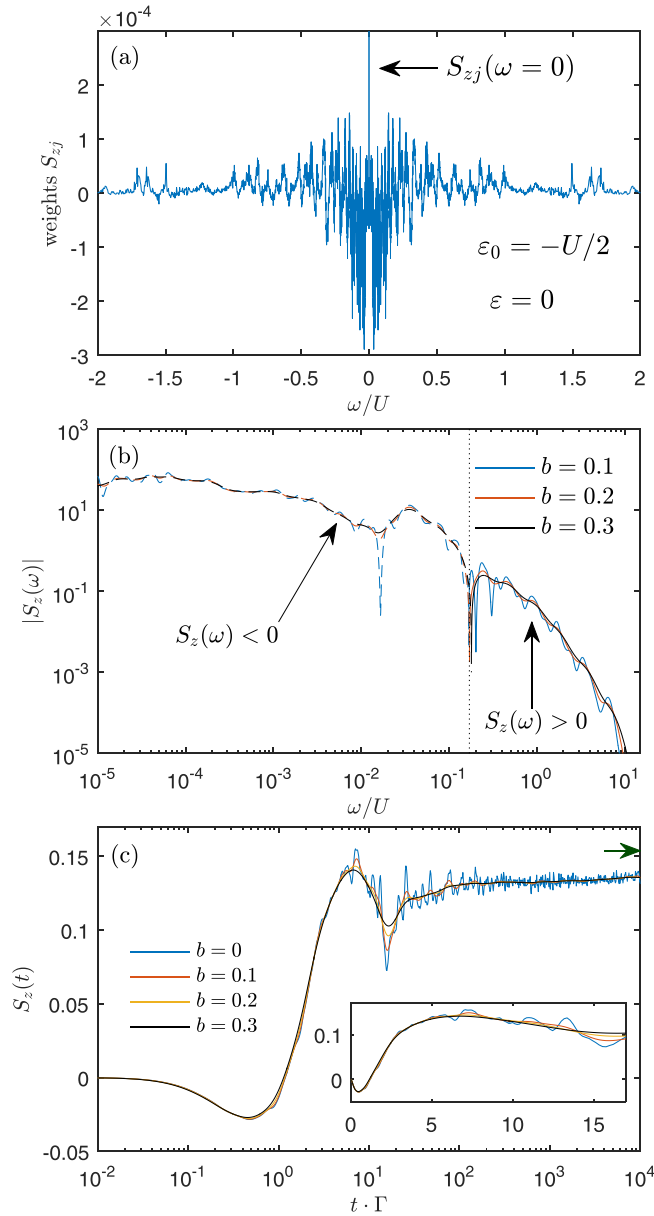


FIG. 5. The same as in Fig. 4 calculated for the dot's magnetization $S_z(t)$. The vertical dotted line in (b) marks the frequency at which the spectral density $S_z(\omega)$ changes sign: For $\omega/U \gtrsim 0.2$, $S_z(\omega) > 0$ (solid lines), while for $\omega/U \lesssim 0.2$, $S_z(\omega) < 0$ (dashed lines). The green arrow in (c) indicates the long-time-limit value of the dot's magnetization.

A. Quench in the coupling strength

In this section, we consider an initially ($t < 0$) unpolarized quantum dot decoupled from the lead, i.e., $S_z(t < 0) = 0$ and $\Gamma_0 = 0$. The initial occupation number depends only on the position of the dot's energy level ε , which in an experimental setup can be tuned by changing the electrostatic potential of the corresponding gate. At time $t = 0$, the coupling Γ between the quantum dot and the ferromagnetic lead is abruptly switched on. Because of that, the spin-resolved charge fluctuations between the dot and the lead become allowed, resulting

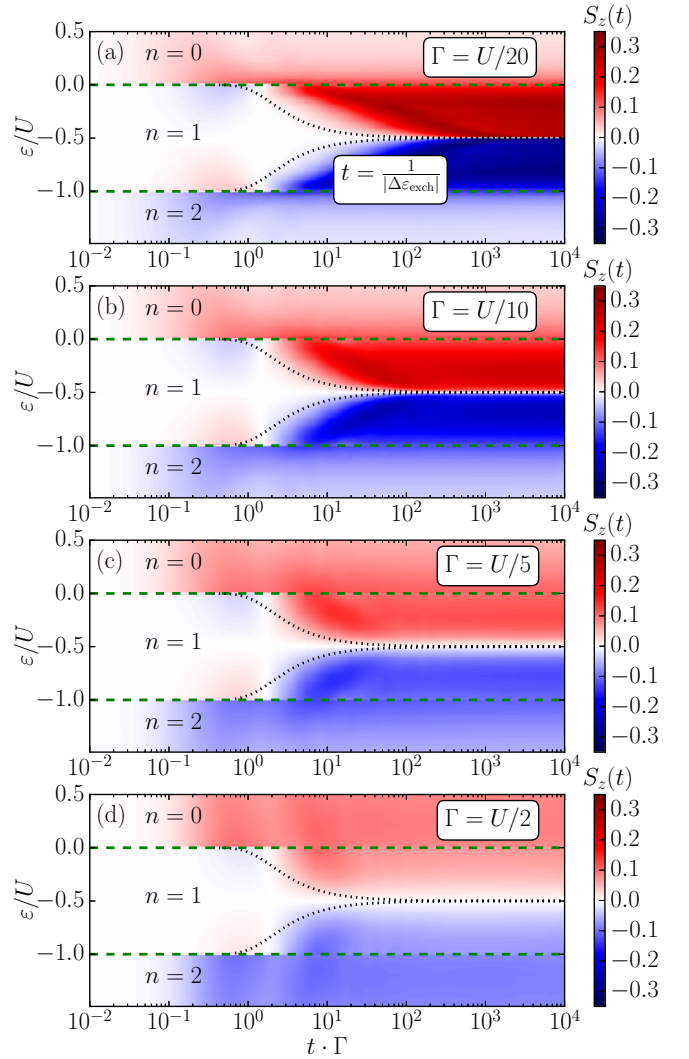


FIG. 6. The quantum dot magnetization $S_z(t)$ after the quench from an isolated and spin-unpolarized quantum dot to the coupled regime, as a function of time and the dots' energy level ε/U for different values of the coupling strength Γ , as indicated. The horizontal green-dashed lines separate regimes with different initial occupation number n . The black dotted lines indicate the timescale associated with the development of the exchange field $t = 1/|\Delta\varepsilon_{\text{exch}}|$. The calculations were performed for $T = 0$, $U = 0.12$ (in units of band half-width), $p = 0.5$, and the following NRG parameters: $\Lambda = 2$, $N_K = 2000$, $N_z = 8$, and $b = 0.3$.

in a spin-dependent renormalization of the quantum dot level, which gives rise to its finite magnetization.

1. Quantum dot's magnetization

The quantum dot magnetization $S_z(t)$ as a function of time and the position of the dot's energy level ε is shown in Fig. 6 for a few values of the coupling strength Γ . The time evolution is calculated for a wide range of position of the dot's energy level, $-1.5 \leq \varepsilon/U \leq 0.5$, therefore we are able to analyze in the full parameter space how the initial occupation of the quantum dot influences the spin dynamics after the quench in the coupling. In general, one can clearly distinguish three regimes with the quantum dot initially occupied by

zero ($n = 0$), one ($n = 1$), and two ($n = 2$) electrons. The different occupation regimes are correspondingly indicated and separated with dashed lines in Fig. 6. Clearly, $S_z(t = 0) = 0$ for all dot occupations, since finite magnetization can build up only due to spin-resolved fluctuations between the dot and ferromagnetic reservoir. Thus, one should expect $S_z(t > 0) \neq 0$. With an even number of electrons occupying the quantum dot in the initial state, the time-dependent magnetization $S_z(t)$ develops in time acquiring only positive values for $n = 0$ ($\varepsilon > 0$) and negative values for $n = 2$ ($\varepsilon < -U$) occupation numbers. Except for the opposite sign (direction of the magnetization), the time evolution of magnetization is identical in both occupation regimes. Apparently, when the quantum dot is either empty or doubly occupied, the growth of the magnetization should not be possible. However, finite coupling Γ renormalizes and broadens the dot's energy level, which for the initially empty quantum dot results in a small growth of occupation $n(t > 0) > 0$, while for the initially doubly occupied dot it leads to the corresponding decrease of the occupation $n(t > 0) < 2$. Moreover, the spin dependence of the coupling strength lifts the degeneracy of singly occupied states, which as a consequence gives rise to a finite magnetization of the quantum dot.

This nonzero magnetization is a direct manifestation of the so-called exchange field that builds up in the quantum dot coupled to a reservoir of the spin-polarized electrons [56]. The exchange field can be defined as $\Delta\varepsilon_{\text{exch}} = \delta\varepsilon_{\uparrow} - \delta\varepsilon_{\downarrow}$, where $\delta\varepsilon_{\sigma}$ is the renormalization of the spin- σ dot level caused by the spin-dependent charge fluctuations. The renormalization can be estimated within the second-order perturbation theory as [56–59]

$$\Delta\varepsilon_{\text{exch}} = \frac{2p\Gamma}{\pi} \text{Re}[\phi(\varepsilon) - \phi(\varepsilon + U)], \quad (23)$$

with $\phi(\varepsilon) = \Psi(1/2 + i\varepsilon/2\pi T)$, where $\Psi(z)$ is the digamma function. At zero temperature, the formula for the exchange field simply becomes $\Delta\varepsilon_{\text{exch}} = \frac{2p\Gamma}{\pi} \ln|\frac{\varepsilon}{\varepsilon+U}|$. Now, it can be clearly seen that $\Delta\varepsilon_{\text{exch}}$ changes sign exactly at the particle-hole symmetry point, $\varepsilon = -U/2$. Consequently, for $\varepsilon > -U/2$ ($\varepsilon < -U/2$) one finds $\Delta\varepsilon_{\text{exch}} < 0$ ($\Delta\varepsilon_{\text{exch}} > 0$), which immediately implies that $S_z(t) > 0$ [$S_z(t) < 0$] in the corresponding transport regime. This behavior is clearly visible in Fig. 6 in the even dot occupation regimes.

Let us now consider the most interesting regime where initially the quantum dot is occupied by a single electron, i.e., for $-U < \varepsilon < 0$. As can be seen, the general tendency of the behavior of $S_z(t)$ in the long-time limit is consistent with the behavior of the exchange field discussed above. Exactly at the particle-hole symmetry point, the charge fluctuations are the same for both spin directions such that $\delta\varepsilon_{\uparrow} = \delta\varepsilon_{\downarrow}$ and $\Delta\varepsilon_{\text{exch}} = 0$ [56,57]. This is why for $\varepsilon = -U/2$ the magnetization does not develop and the dot remains unpolarized irrespective of time evolution, $S_z(t) = 0$. However, when the energy of the orbital level is moved away from the particle-hole symmetry point, the time evolution of magnetization $S_z(t)$ shows a qualitatively different dependence. For shorter times, $0.1 \lesssim t\Gamma \lesssim 1$, the magnetization points in the direction opposite to its long-time-limit value. Around $t \approx 1/\Gamma$, the sign change of magnetization occurs and subsequently $S_z(t)$ grows and saturates at longer times; see Fig. 6. One could

expect that the timescale for the development of the dot's magnetization (the exchange field) is simply given by $t \sim 1/\Delta\varepsilon_{\text{exch}}$. This is, however, not entirely correct. We would like to point out that the estimation of the magnetization development timescale simply by $t = 1/|\Delta\varepsilon_{\text{exch}}|$ (see the black dotted lines in all panels of Fig. 6) does not fit to the numerically calculated dependence. It is clearly visible that the dynamics of the exchange field development is strongly influenced by the coupling strength and does not scale linearly with Γ .

The comparison of the results for $S_z(t)$ when the coupling strength Γ is varied brings further important observations. In the empty or doubly occupied dot regime, the magnitude of magnetization becomes enhanced with increasing coupling strength. This is associated with an increase of level broadening and renormalization effects as Γ is increased. These effects enlarge the occupation of the odd-electron states, which is responsible for enhancement of $|S_z(t)|$; see Fig. 6. However, as the occupation of odd-electron states becomes enhanced in the even valleys, the same happens for even-occupation states in the odd-electron valley. More precisely, in the singly occupied dot regime, as the coupling strength increases, the occupation of even-electron states becomes enhanced at the cost of the odd states. Consequently, in this transport regime one observes an opposite effect, i.e., the larger the coupling becomes, the smaller is the magnetization that develops in time.

In addition, in the strong-coupling regime also the Kondo correlations come into play. Their role is reflected in the fact that now one needs to detune the dot level more from the particle-hole symmetry point to obtain a considerable magnetization. As is known from the studies of equilibrium transport properties of quantum dots [56–59,64], the Kondo resonance becomes suppressed when detuning from the particle-hole symmetry point becomes so large that the following condition is fulfilled: $|\Delta\varepsilon_{\text{exch}}| \gtrsim T_K$, where T_K is the Kondo temperature. This fact also has strong consequences for the dynamical behavior of the system. Finite values of $S_z(t)$ develop only when the above inequality becomes satisfied, as otherwise the spin of the dot forms a delocalized singlet state with conduction electrons and the magnetization does not develop.

It is important to note that the variation of the coupling strength also has an important impact on the corresponding timescales for the development of the dot's magnetization. For smaller values of the coupling, see Fig. 6(a), it takes a longer time for the magnetization to fully develop, whereas for stronger couplings this timescale becomes reduced; see Fig. 6(d).

2. Buildup of exchange field

Let us now focus on the timescales associated with the development of the dot's magnetization and the associated exchange field. To estimate the magnitude of the exchange field, we compare the value of the time-dependent magnetization calculated with tNRG to the static magnetization of a similar system coupled to normal metallic leads in the presence of an external magnetic field B , i.e., $S_z(t) = \langle S_z(B) \rangle$. The $\langle S_z(B) \rangle$ dependence is calculated with the static NRG procedure for a wide range of magnitudes of external magnetic field B , separately for each presented coupling strength Γ . To solve

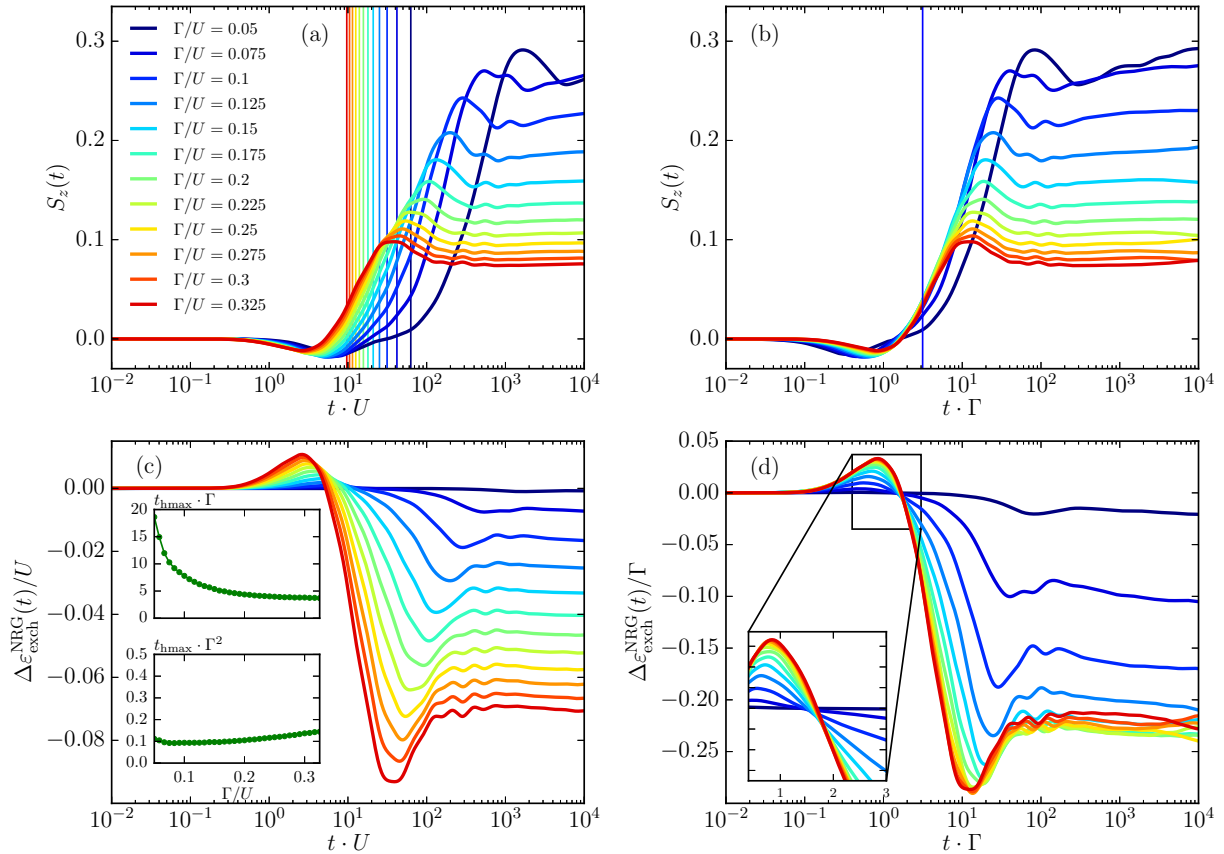


FIG. 7. Top row: The quantum dot magnetization $S_z(t)$; bottom row: the induced exchange field $\Delta\varepsilon_{\text{exch}}^{\text{NRG}}(t)$ after the quench in the coupling strength plotted as a function of time calculated for different couplings, as indicated. The vertical lines in (a) and (b) indicate the timescale associated with the exchange field, $t = 1/|\Delta\varepsilon_{\text{exch}}|$; cf. Eq. (23). The inset in (c) presents the timescale t_{hmax} associated with the half-maximum value of $|\Delta\varepsilon_{\text{exch}}^{\text{NRG}}(t)|$ plotted as a function of Γ , whereas the inset in (d) shows a closeup of $\Delta\varepsilon_{\text{exch}}^{\text{NRG}}(t)$ for times where the sign change of the exchange field occurs. The parameters are the same as in Fig. 6 with the quantum dot's energy level equal to $\varepsilon = -U/4$.

this model at equilibrium, we assume vanishing spin polarization of the leads $p = 0$ and add the Zeeman energy term $H_B = g\mu_B B S_z$ to the quantum dot Hamiltonian H_{QD} , with $g\mu_B \equiv 1$. We then associate the Zeeman energy that results in magnetization $\langle S_z(B) \rangle = S_z(t)$ with the exchange field energy $\Delta\varepsilon_{\text{exch}}^{\text{NRG}}$. In this manner, we are able to evaluate the time dependence of the generated exchange field $\Delta\varepsilon_{\text{exch}}^{\text{NRG}}(t)$.

Figure 7 presents the time evolution of the magnetization [Figs. 7(a) and 7(b)] together with the evaluated exchange field [Figs. 7(c) and 7(d)]. In this figure, the energy of the orbital level is set to $\varepsilon = -U/4$, corresponding to the regime where finite magnetization develops and its sign change as the time elapses is visible; cf. Fig. 6. To get information about the relevant timescales, we plot the dependence of the quantities of interest versus tU [Figs. 7(a) and 7(c)] and $t\Gamma$ [Figs. 7(b) and 7(d)]. In addition, we also mark the timescale associated with exchange field, $t = 1/|\Delta\varepsilon_{\text{exch}}|$, with vertical lines.

It can be seen in the time evolution of magnetization that, independently of the coupling strength, a minimum occurs at times $1 \lesssim tU \lesssim 10$ or $10^{-1} \lesssim t\Gamma \lesssim 1$, where the magnetization points in the opposite direction compared to its long-time-limit value. Subsequently, a strong growth of magnetization is present and the saturation is reached around $tU \gtrsim 10^2$ or $t\Gamma \gtrsim 10$. The comparison of this behavior

between panels (a) and (b) indicates that the buildup of magnetization, i.e., the time at which magnetization starts growing, to a good approximation scales linearly with Γ . Moreover, the saturation of magnetization also exhibits the dynamics strongly dependent on Γ , and for most considered values of the coupling, the maximum magnetization is achieved at times $10 \lesssim t\Gamma \lesssim 10^2$; see Figs. 7(a) and 7(b).

Let us now discuss the time evolution of the evaluated exchange field $\Delta\varepsilon_{\text{exch}}^{\text{NRG}}(t)$. First of all, one can see that the sign of the exchange field is opposite to that of the induced magnetization, i.e., we find $\Delta\varepsilon_{\text{exch}}^{\text{NRG}} > 0$ for $10^{-1} \lesssim tU \lesssim 10$ and $\Delta\varepsilon_{\text{exch}}^{\text{NRG}} < 0$ for $tU \gtrsim 10$; see Fig. 7(c). Furthermore, as in the case of magnetization decreasing the coupling strength generally results in larger values of $S_z(t)$, it has an opposite effect on the generated exchange field. It can be seen that the maximum value of $|\Delta\varepsilon_{\text{exch}}^{\text{NRG}}(t)|$ decreases with lowering Γ . This is in fact quite intuitive—the larger the coupling to the ferromagnetic contact becomes, the larger is the generated exchange field. Note, however, that for weaker couplings a relatively low exchange field is sufficient to induce large magnetization in the quantum dot; see Fig. 7(c).

To identify the relevant timescales for the sign change and the buildup of the exchange field, in Fig. 7(d) we show $\Delta\varepsilon_{\text{exch}}^{\text{NRG}}(t)/\Gamma$ plotted as a function of $t\Gamma$. As can be seen in the inset, which presents the closeup of $\Delta\varepsilon_{\text{exch}}^{\text{NRG}}(t)$ where the sign

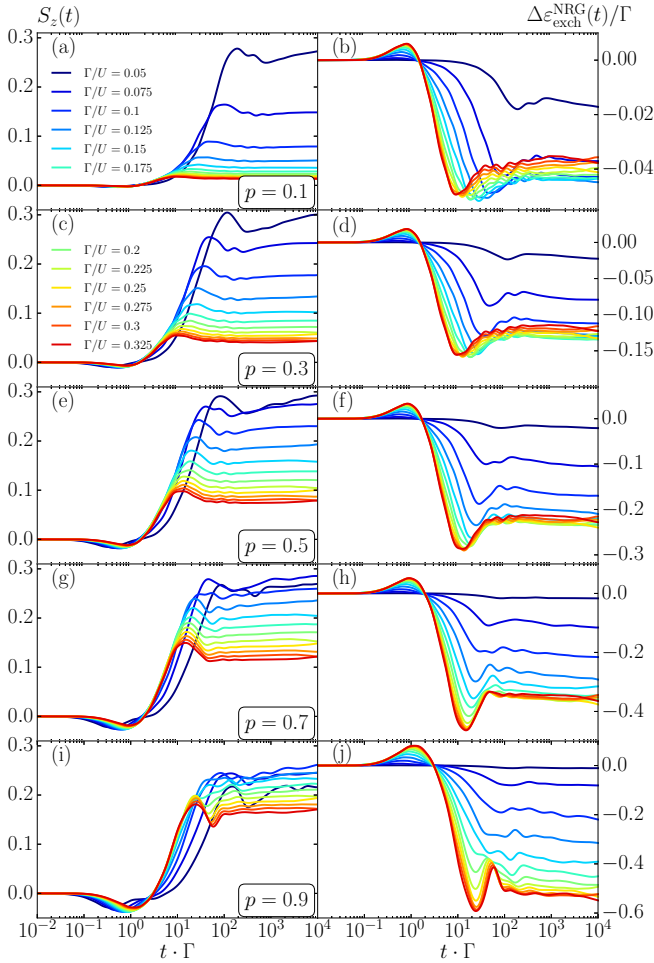


FIG. 8. Left column: The time-dependent magnetization $S_z(t)$; right column: the generated exchange field $\Delta \varepsilon_{\text{exch}}^{\text{NRG}}(t)$ after the quench from an isolated quantum dot to the coupled regime calculated for different values of coupling strength Γ and the lead's spin polarization p , as indicated. The parameters are the same as in Fig. 7.

change occurs, $\Delta \varepsilon_{\text{exch}}^{\text{NRG}}(t) \approx 0$ for $t\Gamma \approx 1$, i.e., the sign change of the exchange field develops for times of the order of $t \approx 1/\Gamma$. On the other hand, it is also visible that the time at which $|\Delta \varepsilon_{\text{exch}}^{\text{NRG}}(t)|$ reaches its maximum does not scale linearly with Γ . To estimate what the scaling is, we determine the time t_{hmax} at which the absolute value of the exchange field reaches half of its maximum value, $|\Delta \varepsilon_{\text{exch}}^{\text{NRG}}(t_{\text{hmax}})| \equiv \max\{|\Delta \varepsilon_{\text{exch}}^{\text{NRG}}(t)|\}/2$. In the inset of Fig. 7(c), we present both $t_{\text{hmax}}\Gamma$ and $t_{\text{hmax}}\Gamma^2$ as a function of the coupling strength. As results from these curves, the time associated with the development of the exchange field scales rather as $t_{\text{hmax}} \propto \frac{1}{\Gamma^2}$ and not as $t_{\text{hmax}} \propto \frac{1}{\Gamma}$. This result is in fact quite counterintuitive, since from Eq. (23) one could expect linear scaling of $\Delta \varepsilon_{\text{exch}}^{\text{NRG}}(t)$ with the coupling strength.

3. Influence of spin polarization

The influence of the spin polarization p of the ferromagnetic contact on the spin dynamics is also nontrivial. Figure 8 presents the time evolution of the magnetization (left column) and the exchange field (right column) for different values of p and Γ . For relatively small values of spin polarization,

i.e., $p \lesssim 0.3$ [see panels (a) and (b) in Fig. 8], neither the magnetization nor the exchange field exhibits the sign change as a function of time. This effect emerges once the spin polarization becomes considerable; see the curves for $p \gtrsim 0.5$ in Fig. 8. Moreover, with increasing p , the values of $S_z(t)$ and $\Delta \varepsilon_{\text{exch}}^{\text{NRG}}(t)$ opposite to their long-time limits are increased. Interestingly, the highest value of magnetization is obtained for rather small values of Γ , almost independently of the spin polarization p . Larger values of the coupling strength result in a faster dynamics (the saturation occurs at earlier times), but on the other hand, the long-time-limit value of magnetization gets lowered. With increasing p , it is evident that the long-time limit of magnetization and exchange field is enhanced, even for strong couplings; see Fig. 8. Furthermore, one can clearly see that the magnitude of the exchange field becomes enhanced upon increasing the spin polarization. In addition, for large values of p the exchange field $\Delta \varepsilon_{\text{exch}}^{\text{NRG}}(t)$ depends more on the value of the coupling Γ ; cf. Figs. 8(b) and 8(j).

4. Quantum dot's occupations

Because one of the most interesting effects discussed here is the sign change of magnetization and the associated exchange field, let us now focus on discussing the mechanism responsible for this effect. It turns out that the analysis of the expectation values of the corresponding occupation operators $n(t)$, $n_{\uparrow}(t)$, and $n_{\downarrow}(t)$ can provide more detailed information about the spin dynamics of the system. Figure 9 presents the dot's occupations $n(t)$, $n_{\uparrow}(t)$, and $n_{\downarrow}(t)$ calculated for different values of the ferromagnetic contact's spin polarization. For comparison, we also show the time evolution of the dot's magnetization $S_z(t)$. Clearly, increasing the spin polarization results in higher values of magnetization in the long-time limit. However, as already emphasized in the previous section, the most interesting dynamics takes place at times around $t \approx 1/\Gamma$, and it is generally associated with the difference between the spin-resolved couplings Γ^{\uparrow} and Γ^{\downarrow} to the ferromagnetic contact.

First of all, one can see that the decrease of the total occupation $n(t)$ after the quench is similar, both qualitatively and quantitatively, for all considered values of p . This decrease is a consequence of the renormalization of the quantum dot level and its broadening due to the coupling to the external reservoir. Note that in the figure $\varepsilon = -U/4$, such that $n(t > 0) < 1$. It is thus clear that once the coupling is turned on, the total occupation number of the dot becomes lowered as the time elapses and it happens at a short timescale, i.e., $n(t)$ starts decreasing when $t\Gamma \approx 10^{-1}$, and for $t\Gamma \approx 1$ the total occupation is already approximately equal to its long-time value; see Fig. 9. It is, however, very important to consider how this precisely happens as far as the spin-resolved occupations are concerned. Because for finite p the spin-up level is coupled more strongly than the spin-down one, it is the spin-up level that reacts first to the switching-on of the coupling. Thus, at a short timescale, the occupation decrease is mostly conditioned by the coupling Γ^{\uparrow} , which leads to lowering of the occupation of the spin-up dot level. However, eventually, the opposite spin component with weaker coupling Γ^{\downarrow} comes into play and determines the dynamics of the system, lowering its occupation accordingly, as the magnetization grows and saturates for

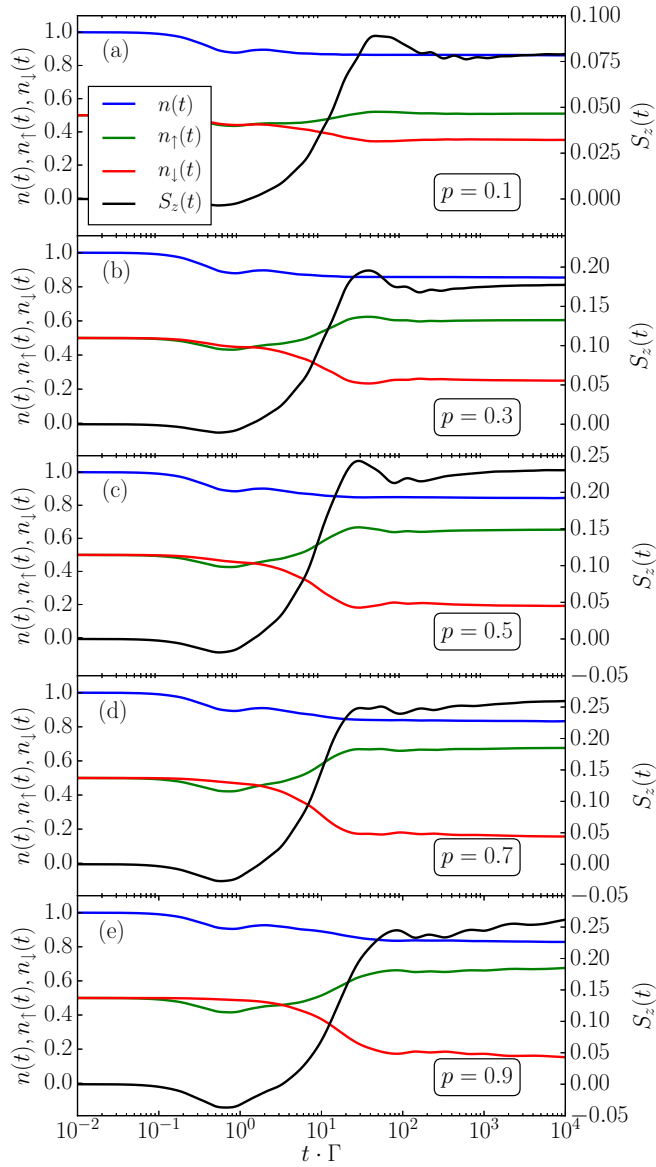


FIG. 9. The time-dependent expectation value of the local operators, $n(t)$, $n_\sigma(t)$, and $S_z(t)$, after the quench in the coupling strength calculated for selected values of the spin polarization of ferromagnetic contact p . The other parameters are the same as in Fig. 7 with $\Gamma = U/10$.

longer times. This can be clearly seen in Fig. 9, especially for larger spin polarizations—the drop of the total occupation is mainly due to the decrease of $n_\uparrow(t)$, such that one observes $n_\uparrow(t) < n_\downarrow(t)$ in a certain range of time. However, as the time goes by, the spin dependence of charge fluctuations finally results in equilibration, such that $n_\uparrow(t) > n_\downarrow(t)$.

In other words, the charge dynamics of the system is governed by the stronger coupling to the majority-spin subband Γ^\uparrow , whereas the spin dynamics is determined by the weaker coupling to the minority-spin subband Γ^\downarrow . Consequently, one observes a sign change of the magnetization (and the induced exchange field) with the time range of magnetization opposite to its long-time-limit value increased upon enhancing the spin polarization p ; see Fig. 9.

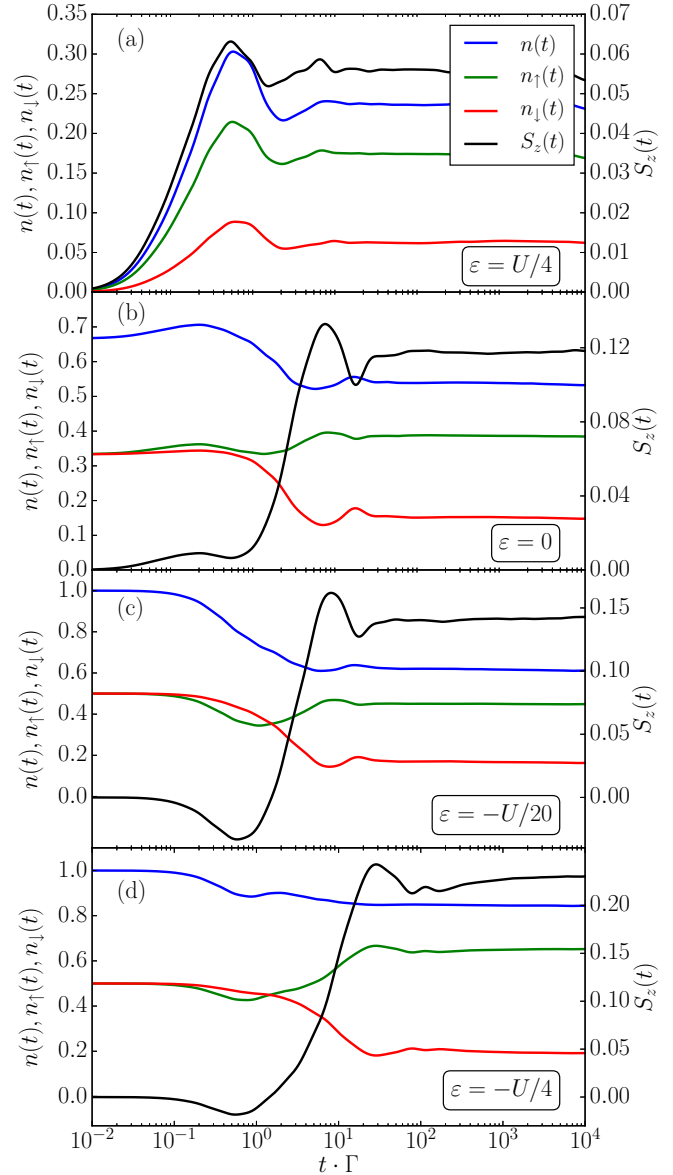


FIG. 10. The time-dependent expectation value of local operators after the quench in the coupling strength calculated for different values of the dot's energy level ε , as indicated, and for other parameters the same as in Fig. 7 with $\Gamma = U/10$.

In Fig. 10 we show the relevant time evolution of the local operators after the quench performed in the coupling strength calculated for four different positions of the dot's energy level. When in the initial state the quantum dot is empty, see the case of $\varepsilon = U/4$ in Fig. 10(a), the total occupation grows from $n(t=0) = 0$ to around $n(t \rightarrow \infty) \approx 0.25$ in the long-time limit. Finite occupation after the quench is possible due to the renormalization and broadening of the dot's energy level. Due to the spin-dependent coupling, the occupation of the spin-up component is higher with respect to the spin-down one, i.e., $n_\uparrow(t) > n_\downarrow(t)$, which holds for all times $t > 0$. As a consequence, the magnetization acquires only positive values $S_z(t) > 0$ and does not change sign at any positive time. A similar behavior is in fact observed for $\varepsilon \geq 0$. For $\varepsilon = 0$ [see Fig. 10(b)], the initial occupation is nonzero,

i.e., $n(0) = 2/3$. Then, switching on the coupling to the lead results in the renormalization that decreases the average occupation number, such that $n(t \rightarrow \infty) \approx 1/2$. Note, however, that when the coupling is turned on, the total occupation first starts increasing slightly and then decreases to reach one-half. The behavior of $n(t)$ is reflected in the dependence of the spin-resolved occupations. The occupation of $n_{\uparrow}(t)$ exhibits small fluctuations as a function of time, but in the long-time limit it acquires a value relatively close to the initial one, $n_{\uparrow}(t \rightarrow \infty) \approx 0.4$. On the other hand, the evolution of $n_{\downarrow}(t)$ is strongly correlated with the total occupation $n(t)$. As a result, in this transport regime, the dot's magnetization is always positive.

However, when the energy of the orbital level is lowered further such that in the initial state the dot is occupied by a single electron, the spin dynamics gets qualitatively new features; see Figs. 10(c) and 10(d). As already explained earlier, now the important effect of the renormalization and broadening due to switching-on of the coupling is that the average occupation of the quantum dot is decreased [$n(t) < 1$] with respect to the initial state. Moreover, the evolution of the system is now governed by two timescales: while the first one, $t \sim 1/\Gamma^{\uparrow}$, is responsible for charge dynamics, the second one, $t \sim 1/\Gamma^{\downarrow}$, determines the magnetization dynamics. The interplay between the two spin-resolved components of occupation results in the oscillations of magnetization as a function of time with the corresponding sign change.

B. Quench in the orbital level position

In this section, we consider the quench performed in the position of the quantum dot orbital level. The dot is coupled to the ferromagnetic lead before the quench, and the coupling strength remains unchanged, i.e., $\Gamma_0 = \Gamma$. The parameter that is abruptly switched at time $t = 0$ is the dot's energy level $\varepsilon_0 \rightarrow \varepsilon$. We study the time evolution of the dot's occupation number (Fig. 11) and magnetization (Fig. 12) after the corresponding quench. We consider four different initial energy levels ε_0 , and the corresponding expectation values are calculated for a wide range of final level position ε . Here, it is important to note that the value of ε_0 determines the quantum dot initial occupation number and magnetization.

As can be seen in Fig. 11, the short time evolution of the occupancy is mainly dependent on the initial occupation. In all the considered cases, the occupation monotonically approaches saturation at times $t \approx 1/\Gamma$. Further behavior for times $t \gtrsim 1/\Gamma$ is qualitatively similar across all values of ε_0 considered, and for all final level positions ε approaches the long-time limit. We note that there might occur a small deviation of the long-time-limit value from the thermodynamic value, which depends on the difference in energy between the initial and final Hamiltonians. This is associated with the fact that the larger this difference is, the more difficult it is for the system to dissipate energy in the long-time limit, which is a direct consequence of the fact that the system does not fully thermalize on the finite Wilson chain [43,76]. When the quench has a relatively large energy difference, i.e., $|\varepsilon_0 - \varepsilon| \gtrsim U$, an oscillatory behavior is visible right after attaining the maximum value at times $1 \lesssim t\Gamma \lesssim 10$ for $\varepsilon/U \lesssim -1$ and $\varepsilon/U \gtrsim 0.5$; see Figs. 11(c) and 11(d).

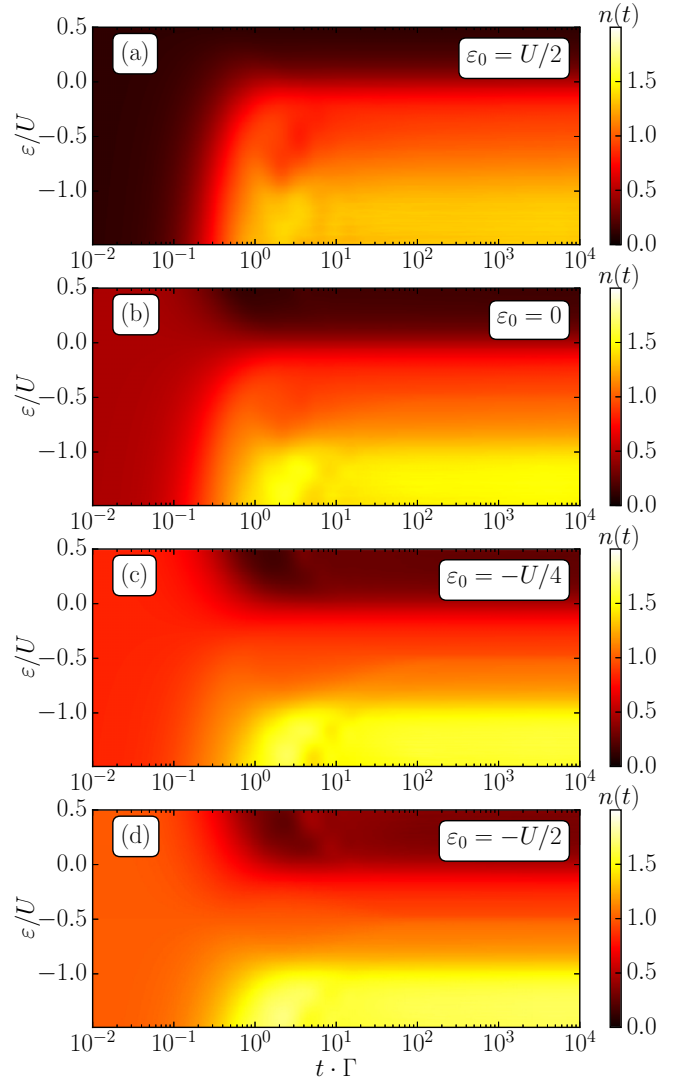


FIG. 11. The time-dependent occupation number $n(t)$ after performing the quench in the quantum dot's orbital level position from ε_0 to ε . The other parameters are the same as in Fig. 7 with $\Gamma = U/10$.

The quench dynamics is even more interesting when the time evolution of the quantum dot's magnetization $S_z(t)$ is considered. Now, the initial position of the dot's energy level ε_0 strongly determines the behavior of the magnetization for short times ($t\Gamma \lesssim 10^{-1}$). In general, independently of the initial conditions, for the final values of the energy level above the particle-hole symmetry point, i.e., $\varepsilon > -U/2$, the quantum dot acquires magnetization, which is parallel to the magnetization of the ferromagnet. For the particle-hole symmetry point ($\varepsilon = -U/2$), the exchange field vanishes and the magnetization does not develop. On the other hand, for the dot level position below the particle-hole symmetry point, $\varepsilon < -U/2$, the exchange field changes sign and the quantum dot is magnetized in the opposite direction.

Let us now discuss the system's dynamics in more detail and focus on the influence of the initial condition, i.e., the value of ε_0 , on the time dependence of the dot's occupation and magnetization. For the orbital level set above the Fermi

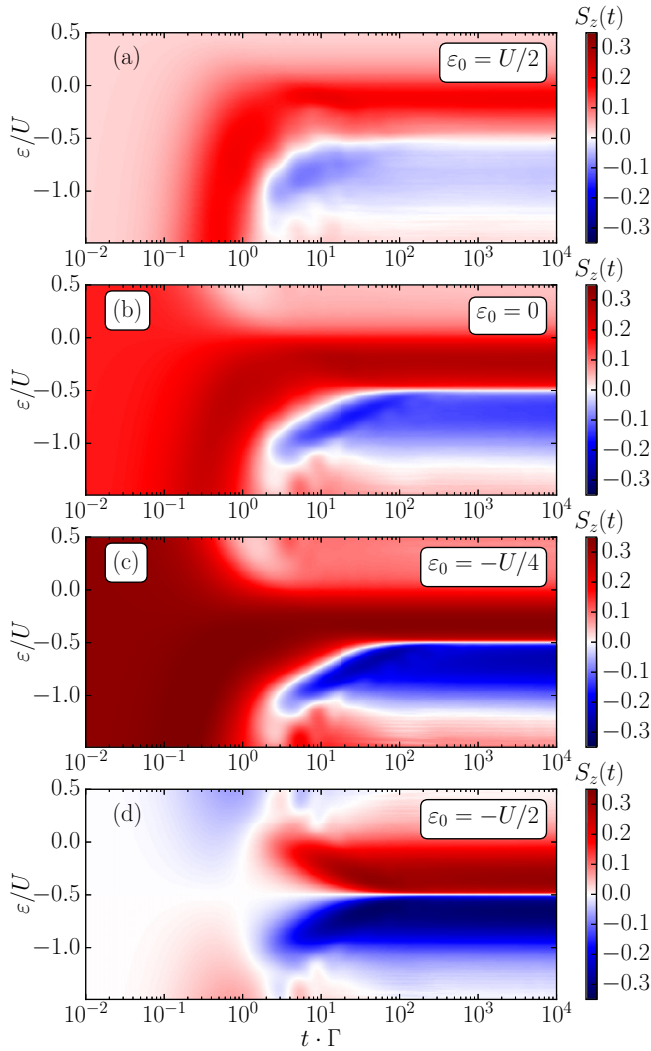


FIG. 12. The time-dependent magnetization $S_z(t)$ of the dot after performing the quench in the orbital level from ε_0 to ε . The other parameters are the same as in Fig. 7 with $\Gamma = U/10$.

level, see Fig. 11(a) where $\varepsilon_0 = U/2$, the initial occupation of the quantum dot is small but finite, $n(0) \approx 0.1$, which results in a finite magnetization in the direction of the magnetization of the ferromagnetic lead; see Fig. 12(a). At times $t\Gamma \gtrsim 10^{-1}$, the magnetization starts to grow. Further time dependence of S_z significantly depends on the final level position ε . For $\varepsilon > 0$, the quantum dot increases mildly and monotonically its occupation number, and, accordingly, the magnetization grows in a similar manner. However, when $0 > \varepsilon > -U/2$, the magnetization buildup is rapid compared to the previous regime, which is due to a higher occupation number $n(t) \approx 1$. Here, the dynamics of charge and spin are very similar as both average expectation values saturate at times $t \approx 1/\Gamma$. On the other hand, for $\varepsilon < -U/2$, the system magnetizes in the opposite direction. Now, when the initial position of the dot level is shifted toward lower energies, see Figs. 11(b) and 11(c) and Figs. 12(b) and 12(c), one can observe two effects. First, the initial magnetization is stronger as ε_0 is lowered, which is due to an increased occupation at the initial

state. This is visible down to the particle-hole symmetry point; cf. Figs. 11(d) and 12(d). Secondly, the long-time-limit magnetization is strongly enhanced. When lowering the initial position of the orbital level further, the quench is performed from the lower-energy state, and therefore it is easier for the system to achieve the thermal average in the long-time limit.

Finally, we consider the case when the dot is set at the particle-hole symmetry point in the initial state, where $S_z(t=0) = 0$. In general, in this case the spin dynamics is antisymmetric with respect to detuning from the particle-hole symmetry point; see Fig. 12(d). The quantum dot is initially spin-unpolarized, $S_z(0) = 0$, and for a wide range of the final position of the orbital level energy ε it starts to build up magnetization for times $10^{-1} \lesssim t\Gamma \lesssim 1$ in the opposite direction to its long-time-limit value. Consequently, for times $1 \lesssim t\Gamma \lesssim 10$, there is at least one sign change present in the case of $0 < \varepsilon/U < -1$ (except for the particle-hole symmetry point and its vicinity). Moreover, an oscillatory behavior of the magnetization takes place in the case of stronger quenches, i.e., for $\varepsilon > 0$ or $\varepsilon < -U$. In the above regimes of ε , the absolute value of the long-time limit of magnetization is also lower compared to the magnetization in the singly occupied regime; see Fig. 12(d). The long-time-limit value of the dot's magnetization is fully suppressed in the cases of a doubly occupied and empty quantum dot $S_z(t \rightarrow \infty) = 0$, which is visible for $\varepsilon = U/2$ and $\varepsilon = -3U/2$ in Fig. 12(d).

C. Finite-temperature effects

Let us now consider the influence of finite temperature T on the dynamics of the system, which undergoes quenches discussed in the preceding sections. We focus on the most interesting case with a single electron occupying the quantum dot. Figure 13 presents the time evolution of local operators after the quench in the coupling strength calculated for different values of temperature T expressed in units of Γ ($k_B \equiv 1$). It can be seen that at zero temperature the dot occupation decreases slightly due to the fact that the system is detuned from the particle-hole symmetry point ($\varepsilon = -U/4$ in the figure). The different time dependence of the spin-resolved occupations results in finite magnetization, which changes sign around $t \approx 1/\Gamma$, as explained in the previous sections. When the temperature is increased, the long-time value of the magnetization becomes strongly suppressed, and for temperatures of the order of the coupling strength, $S_z(t) \approx 0$. This is associated with the fact that the spin-resolved charge fluctuations become overwhelmed by thermal fluctuations, which essentially suppress the system dynamics once $t \gtrsim 1/T$. More specifically, upon increasing the temperature, the difference in the total occupation between the initial and final states drops strongly; see Fig. 13(b). For $T = 0$, the quench modifies the occupation number from $n(t=0) = 1$ to $n(t\Gamma > 10) \approx 0.85$, while for finite temperatures the difference between the initial and long-time-limit value of the occupation is much smaller due to enhanced thermal fluctuations. Moreover, thermal fluctuations are responsible for decreasing the difference in the occupation of the spin-up and spin-down components, which is clearly visible when one compares panels (c) and (d) in Fig. 13. This altogether leads to the suppression of the dot's magnetization and, consequently, the induced exchange field.

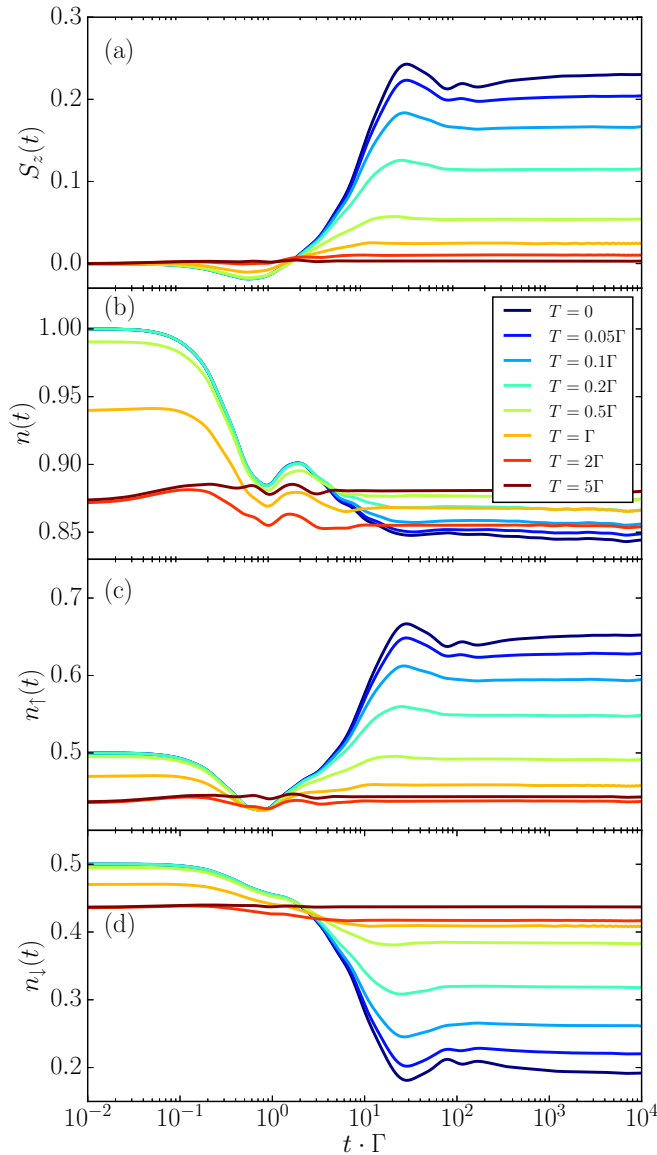


FIG. 13. The expectation values of local operators after the quench in the coupling strength from $\Gamma_0 = 0$ to $\Gamma = U/10$ plotted as a function of time and calculated for different temperatures, as indicated. The other parameters are the same as in Fig. 7.

The case when the quench is performed in the dot's orbital level is presented in Fig. 14. We consider the scenario when initially the system is tuned to the particle-hole symmetry point. Therefore, the initial magnetization is equal to $S_z(t = 0) = 0$, while the occupation number is given by $n(t = 0) = 1$. Then, the orbital level is detuned from this point to $\varepsilon = 0$, such that finite magnetization builds up in the dot as the time elapses. At first, the dependence is qualitatively very similar to the previous case, where the coupling strength was quenched; cf. Figs. 13(a) and 14(a). The long-time limit of magnetization drops as temperature is increased in a similar fashion. However, there is a qualitative difference, since now a higher temperature is necessary to fully suppress the magnetization. This is related to the energy difference between the initial and final Hamiltonians describing the quench, which in the case of

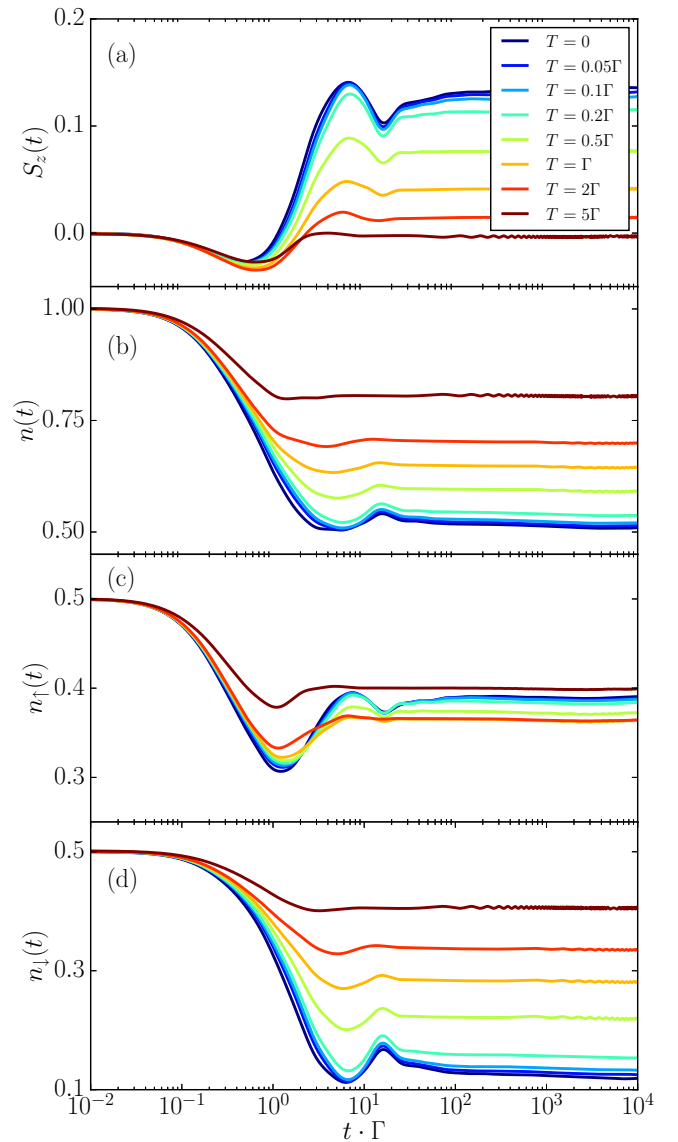


FIG. 14. The same as in Fig. 13 calculated for the quench in the quantum dot occupation from $\varepsilon_0 = -U/2$ to $\varepsilon = 0$. The other parameters are the same as in Fig. 7 with $\Gamma = U/10$.

quench in the orbital level position is larger than in the previous quench by around one order of magnitude. The influence of finite temperature is clearly visible in Fig. 14(b), where the long-time-limit value of the occupation is enhanced with T . As far as the spin-dependent components are concerned, the effect of thermal fluctuations is relatively weak on the spin-up occupation, while it mainly increases the occupation of the spin-down occupation; see Figs. 14(c) and 14(d). Altogether, finite temperature balances both spin-resolved components of the dot's occupation and leads to the drop of the dot's magnetization; see Fig. 14(a).

IV. CONCLUSIONS

In this paper, we have examined the spin-resolved quench dynamics of a correlated quantum dot attached to a reservoir of spin-polarized electrons. The considerations were

performed by using the time-dependent numerical renormalization group method in the matrix product state framework. We studied the system dynamics by considering two types of quantum quenches: the first one was performed in the coupling strength, whereas the second one was performed in the position of the dot's orbital level. The emphasis was put on the analysis of the time-dependent expectation values of local operators, such as the dot's occupation number and magnetization. By comparing the induced magnetization with the expectation value of the dot's spin for nonmagnetic contacts in the presence of magnetic field, we were able to estimate the magnitude of the generated exchange field and analyze its buildup in time. Moreover, by implementing the full density matrix of the system, we have also examined the effects of finite temperature on spin dynamics.

In the case of quench performed in the coupling strength, we carried out a detailed analysis of the influence of the quantum dot initial occupation on the time evolution of the dot's magnetization and occupation. In particular, we found a time range where a sign change occurs during the nonmonotonic buildup of magnetization and the associated induced exchange field. We identified two timescales describing this nontrivial spin dynamics, and we explained this effect by performing a detailed analysis of the time dependence of expectation values of spin-resolved quantum dot occupations. It turned out that while the charge dynamics is mainly governed by the coupling to the majority-spin subband of the ferromagnet, the spin dynamics is mostly determined by the minority-spin-subband coupling. This results in a qualitatively different time dependence of spin-resolved quantum dot occupations, which is revealed through the corresponding sign change of the magnetization.

Furthermore, the case of quench performed in the dot's orbital level position was considered. Similarly to the first type of quench, we accentuated the influence of the system's initial conditions on the system's dynamical behavior. Despite the relatively clear and simple time dependence of the quantum dot total occupancy, we found the spin dynamics to be nontrivial. In particular, we showed that the system quenched from the particle-hole symmetry point exhibits a nonmonotonic behavior of magnetization that can include multiple sign changes.

In addition, we have analyzed the influence of finite temperature on both types of the considered quenches. The thermal fluctuations strongly suppress the dynamics of the system for times $t \gtrsim 1/T$. More specifically, finite temperature is responsible for balancing the spin-up and spin-down components of the quantum dot occupation, which is clearly visible as a drop of the dot's magnetization.

Finally, we note that while the exchange field in the long-time limit can be seen as an effective magnetic field acting on the dot [63], at shorter times, of the order of $t \approx 1/\Gamma$, it results in an interesting dynamical behavior of the system involving a sign change of the quantum dot magnetization. In this case, an intuitive analogy to a simple application of an external magnetic field is rather unjustified.

ACKNOWLEDGMENTS

We gratefully acknowledge discussions with Andreas Weichselbaum. This work was supported by the Polish National Science Centre from funds awarded through the decision No. 2017/27/B/ST3/00621. Computing time at the Poznań Supercomputing and Networking Center is also acknowledged.

-
- [1] S. A. Wolf, D. D. Awschalom, R. A. Buhrman, J. M. Daughton, S. von Molnár, M. L. Roukes, A. Y. Chtchelkanova, and D. M. Treger, Spintronics: A spin-based electronics vision for the future, *Science* **294**, 1488 (2001).
 - [2] I. Žutić, J. Fabian, and S. Das Sarma, Spintronics: Fundamentals and applications, *Rev. Mod. Phys.* **76**, 323 (2004).
 - [3] A. Barenco, D. Deutsch, A. Ekert, and R. Jozsa, Conditional Quantum Dynamics and Logic Gates, *Phys. Rev. Lett.* **74**, 4083 (1995).
 - [4] D. Loss and D. P. DiVincenzo, Quantum computation with quantum dots, *Phys. Rev. A* **57**, 120 (1998).
 - [5] M. B. Menskii, Dissipation and decoherence in quantum systems, *Phys. Usp.* **46**, 1163 (2003).
 - [6] D. Goldhaber-Gordon, H. Shtrikman, D. Mahalu, D. Abusch-Magder, U. Meirav, and M. A. Kastner, Kondo effect in a single-electron transistor, *Nature (London)* **391**, 156 (1998).
 - [7] S. M. Cronenwett, T. H. Oosterkamp, and L. P. Kouwenhoven, A tunable kondo effect in quantum dots, *Science* **281**, 540 (1998).
 - [8] L. Hofstetter, S. Csonka, J. Nygård, and C. Schönberger, Cooper pair splitter realized in a two-quantum-dot y-junction, *Nature (London)* **461**, 960 (2009).
 - [9] S. De Franceschi, L. Kouwenhoven, C. Schönberger, and W. Wernsdorfer, Hybrid superconductor-quantum dot devices, *Nat. Nanotech.* **5**, 703 (2010), review article.
 - [10] A. Yacoby, M. Heiblum, D. Mahalu, and H. Shtrikman, Coherence and Phase Sensitive Measurements in a Quantum Dot, *Phys. Rev. Lett.* **74**, 4047 (1995).
 - [11] A. Donarini, M. Niklas, M. Schafberger, N. Paradiso, C. Strunk, and M. Grifoni, Coherent population trapping by dark state formation in a carbon nanotube quantum dot, *Nat. Commun.* **10**, 381 (2019).
 - [12] L. P. Kouwenhoven, C. M. Marcus, P. L. McEuen, S. Tarucha, R. M. Westervelt, and N. S. Wingreen, *Mesoscopic Electron Transport* (Springer, Dordrecht, 1997), pp. 105–214.
 - [13] S. Loth, M. Etzkorn, C. P. Lutz, D. M. Eigler, and A. J. Heinrich, Measurement of fast electron spin relaxation times with atomic resolution, *Science* **329**, 1628 (2010).
 - [14] Y. Terada, S. Yoshida, O. Takeuchi, and H. Shigekawa, Real-space imaging of transient carrier dynamics by nanoscale pump-probe microscopy, *Nat. Photon.* **4**, 869 (2010).
 - [15] S. Yoshida, Y. Aizawa, Zi-han Wang, R. Oshima, Y. Mera, E. Matsuyama, H. Oigawa, O. Takeuchi, and H. Shigekawa, Probing ultrafast spin dynamics with optical pump-probe scanning tunneling microscopy, *Nat. Nanotech.* **9**, 588 (2014).
 - [16] M. Cetina, M. Jag, R. S. Lous, I. Fritsche, J. T. M. Walraven, R. Grimm, J. Levinsen, M. M. Parish, R. Schmidt, M. Knap, and E. Demler, Ultrafast many-body interferometry of impurities coupled to a fermi sea, *Science* **354**, 96 (2016).
 - [17] C. Latta, F. Haupt, M. Hanl, A. Weichselbaum, M. Claassen, W. Wuester, P. Fallahi, S. Faelt, L. Glazman, J. von Delft,

- H. E. Türeci, and A. Imamoglu, Quantum quench of kondo correlations in optical absorption, *Nature (London)* **474**, 627 (2011).
- [18] F. Haupt, S. Smolka, M. Hanl, W. Wüster, J. Miguel-Sanchez, A. Weichselbaum, J. von Delft, and A. Imamoglu, Nonequilibrium dynamics in an optical transition from a neutral quantum dot to a correlated many-body state, *Phys. Rev. B* **88**, 161304(R) (2013).
- [19] D. C. Langreth and P. Nordlander, Derivation of a master equation for charge-transfer processes in atom-surface collisions, *Phys. Rev. B* **43**, 2541 (1991).
- [20] A. Rosch, J. Paaske, J. Kroha, and P. Wölfle, Nonequilibrium Transport Through a Kondo Dot in a Magnetic Field: Perturbation Theory and Poor Man's Scaling, *Phys. Rev. Lett.* **90**, 076804 (2003).
- [21] S. R. White and A. E. Feiguin, Real-Time Evolution using the Density Matrix Renormalization Group, *Phys. Rev. Lett.* **93**, 076401 (2004).
- [22] M. Schiró and M. Fabrizio, Time-Dependent Mean Field Theory for Quench Dynamics in Correlated Electron Systems, *Phys. Rev. Lett.* **105**, 076401 (2010).
- [23] E. Gull, A. J. Millis, A. I. Lichtenstein, A. N. Rubtsov, M. Troyer, and P. Werner, Continuous-time monte carlo methods for quantum impurity models, *Rev. Mod. Phys.* **83**, 349 (2011).
- [24] D. M. Kennes, S. G. Jakobs, C. Karrasch, and V. Meden, Renormalization group approach to time-dependent transport through correlated quantum dots, *Phys. Rev. B* **85**, 085113 (2012).
- [25] T. L. Schmidt, P. Werner, L. Mühlbacher, and A. Komnik, Transient dynamics of the Anderson impurity model out of equilibrium, *Phys. Rev. B* **78**, 235110 (2008).
- [26] R. Vasseur, K. Trinh, S. Haas, and H. Saleur, Crossover Physics in the Nonequilibrium Dynamics of Quenched Quantum Impurity Systems, *Phys. Rev. Lett.* **110**, 240601 (2013).
- [27] A. E. Antipov, Q. Dong, and E. Gull, Voltage Quench Dynamics of a Kondo System, *Phys. Rev. Lett.* **116**, 036801 (2016).
- [28] E. Greplova, E. A. Laird, G. A. Briggs, and K. Mølmer, Conditioned spin and charge dynamics of a single-electron quantum dot, *Phys. Rev. A* **96**, 052104 (2017).
- [29] N. Fröhling and F. B. Anders, Long-time coherence in fourth-order spin correlation functions, *Phys. Rev. B* **96**, 045441 (2017).
- [30] N. S. Maslova, P. I. Arseyev, and V. N. Mantsevich, Quenched dynamics of entangled states in correlated quantum dots, *Phys. Rev. A* **96**, 042301 (2017).
- [31] P. Haughian, M. Esposito, and T. L. Schmidt, Quantum thermodynamics of the resonant-level model with driven system-bath coupling, *Phys. Rev. B* **97**, 085435 (2018).
- [32] M. Kanász-Nagy, Y. Ashida, T. Shi, C. P. Moca, T. N. Ikeda, S. Fölling, J. I. Cirac, G. Zaránd, and E. A. Demler, Exploring the anisotropic Kondo model in and out of equilibrium with alkaline-earth atoms, *Phys. Rev. B* **97**, 155156 (2018).
- [33] R. Taranko and T. Domański, Buildup and transient oscillations of Andreev quasiparticles, *Phys. Rev. B* **98**, 075420 (2018).
- [34] M. A. Cazalilla and J. B. Marston, Time-Dependent Density-Matrix Renormalization Group: A Systematic Method for the Study of Quantum Many-Body Out-Of-Equilibrium Systems, *Phys. Rev. Lett.* **88**, 256403 (2002).
- [35] S. Kirino, T. Fujii, J. Zhao, and K. Ueda, Time-dependent dmrg study on quantum dot under a finite bias voltage, *J. Phys. Soc. Jpn.* **77**, 084704 (2008).
- [36] H. E. Türeci, M. Hanl, M. Claassen, A. Weichselbaum, T. Hecht, B. Braunecker, A. Govorov, L. Glazman, A. Imamoglu, and J. von Delft, Many-Body Dynamics of Exciton Creation in a Quantum Dot by Optical Absorption: A Quantum Quench Towards Kondo Correlations, *Phys. Rev. Lett.* **106**, 107402 (2011).
- [37] S. Andergassen, M. Pletyukhov, D. Schuricht, H. Schoeller, and L. Borda, Renormalization group analysis of the interacting resonant-level model at finite bias: Generic analytic study of static properties and quench dynamics, *Phys. Rev. B* **83**, 205103 (2011).
- [38] W. Mündler, A. Weichselbaum, M. Goldstein, Y. Gefen, and J. von Delft, Anderson orthogonality in the dynamics after a local quantum quench, *Phys. Rev. B* **85**, 235104 (2012).
- [39] E. Eidelstein, A. Schiller, F. Güttge, and F. B. Anders, Coherent control of correlated nanodevices: A hybrid time-dependent numerical renormalization-group approach to periodic switching, *Phys. Rev. B* **85**, 075118 (2012).
- [40] D. M. Kennes and V. Meden, Quench dynamics of correlated quantum dots, *Phys. Rev. B* **85**, 245101 (2012).
- [41] F. Güttge, F. B. Anders, U. Schollwöck, E. Eidelstein, and A. Schiller, Hybrid nrg-dmrg approach to real-time dynamics of quantum impurity systems, *Phys. Rev. B* **87**, 115115 (2013).
- [42] D. M. Kennes, V. Meden, and R. Vasseur, Universal quench dynamics of interacting quantum impurity systems, *Phys. Rev. B* **90**, 115101 (2014).
- [43] I. Weymann, J. von Delft, and A. Weichselbaum, Thermalization and dynamics in the single-impurity anderson model, *Phys. Rev. B* **92**, 155435 (2015).
- [44] K. Bidzhiev and G. Misguich, Out-of-equilibrium dynamics in a quantum impurity model: Numerics for particle transport and entanglement entropy, *Phys. Rev. B* **96**, 195117 (2017).
- [45] J. Kondo, Resistance minimum in dilute magnetic alloys, *Prog. Theor. Phys.* **32**, 37 (1964).
- [46] A. C. Hewson, *The Kondo Problem to Heavy Fermions* (Cambridge University Press, Cambridge, 1997).
- [47] K. G. Wilson, The renormalization group: Critical phenomena and the kondo problem, *Rev. Mod. Phys.* **47**, 773 (1975).
- [48] F. B. Anders and A. Schiller, Real-Time Dynamics in Quantum-Impurity Systems: A Time-Dependent Numerical Renormalization-Group Approach, *Phys. Rev. Lett.* **95**, 196801 (2005).
- [49] F. B. Anders and A. Schiller, Spin precession and real-time dynamics in the Kondo model: Time-dependent numerical renormalization-group study, *Phys. Rev. B* **74**, 245113 (2006).
- [50] H. T. M. Nghiem and T. A. Costi, Generalization of the time-dependent numerical renormalization group method to finite temperatures and general pulses, *Phys. Rev. B* **89**, 075118 (2014).
- [51] H. T. M. Nghiem and T. A. Costi, Time-dependent numerical renormalization group method for multiple quenches: Application to general pulses and periodic driving, *Phys. Rev. B* **90**, 035129 (2014).
- [52] H. T. M. Nghiem and T. A. Costi, Time-dependent numerical renormalization group method for multiple quenches: towards exact results for the long time limit of thermodynamic observables and spectral functions, *Phys. Rev. B* **98**, 155107 (2018).

- [53] D. Roosen, M. R. Wegewijs, and W. Hofstetter, Nonequilibrium Dynamics of Anisotropic Large Spins in the Kondo Regime: Time-Dependent Numerical Renormalization Group Analysis, *Phys. Rev. Lett.* **100**, 087201 (2008).
- [54] B. Lechtenberg and F. B. Anders, Spatial and temporal propagation of Kondo correlations, *Phys. Rev. B* **90**, 045117 (2014).
- [55] H. T. M. Nghiem and T. A. Costi, Time Evolution of the Kondo Resonance in Response to a Quench, *Phys. Rev. Lett.* **119**, 156601 (2017).
- [56] J. Martinek, Y. Utsumi, H. Imamura, J. Barnaś, S. Maekawa, J. König, and G. Schön, Kondo Effect in Quantum Dots Coupled to Ferromagnetic Leads, *Phys. Rev. Lett.* **91**, 127203 (2003).
- [57] M.-S. Choi, D. Sánchez, and R. López, Kondo Effect in a Quantum Dot Coupled to Ferromagnetic Leads: A Numerical Renormalization Group Analysis, *Phys. Rev. Lett.* **92**, 056601 (2004).
- [58] J. Martinek, M. Sindel, L. Borda, J. Barnaś, R. Bulla, J. König, G. Schön, S. Maekawa, and J. von Delft, Gate-controlled spin splitting in quantum dots with ferromagnetic leads in the kondo regime, *Phys. Rev. B* **72**, 121302(R) (2005).
- [59] M. Sindel, L. Borda, J. Martinek, R. Bulla, J. König, G. Schön, S. Maekawa, and J. von Delft, Kondo quantum dot coupled to ferromagnetic leads: Numerical renormalization group study, *Phys. Rev. B* **76**, 045321 (2007).
- [60] A. N. Pasupathy, R. C. Bialczak, J. Martinek, J. E. Grose, L. A. K. Donev, P. L. McEuen, and D. C. Ralph, The Kondo effect in the presence of ferromagnetism, *Science* **306**, 86 (2004).
- [61] D. Matsubayashi and M. Eto, Spin splitting and Kondo effect in quantum dots coupled to noncollinear ferromagnetic leads, *Phys. Rev. B* **75**, 165319 (2007).
- [62] J. R. Hauptmann, J. Paaske, and P. E. Lindelof, Electric-field-controlled spin reversal in a quantum dot with ferromagnetic contacts, *Nat. Phys.* **4**, 373 (2008).
- [63] M. Gaass, A. K. Hüttel, K. Kang, I. Weymann, J. von Delft, and Ch. Strunk, Universality of the Kondo Effect in Quantum Dots with Ferromagnetic Leads, *Phys. Rev. Lett.* **107**, 176808 (2011).
- [64] I. Weymann, Finite-temperature spintronic transport through Kondo quantum dots: Numerical renormalization group study, *Phys. Rev. B* **83**, 113306 (2011).
- [65] I. Weymann, R. Chirla, P. Trocha, and C. P. Moca, Su(4) Kondo effect in double quantum dots with ferromagnetic leads, *Phys. Rev. B* **97**, 085404 (2018).
- [66] L. I. Glazman and M. E. Raikh, Resonant Kondo transparency of a barrier with quasilocal impurity states, *Pis'ma Zh. Eksp. Teor. Fiz.* **47**, 378 (1988) [*JETP Lett.* **47**, 452 (1988)].
- [67] R. Bulla, T. A. Costi, and T. Pruschke, Numerical renormalization group method for quantum impurity systems, *Rev. Mod. Phys.* **80**, 395 (2008).
- [68] We used the open-access Budapest Flexible DM-NRG code, <http://www.phy.bme.hu/~dmnrg/>; O. Legeza, C. P. Moca, A. I. Tóth, I. Weymann, and G. Zaránd, Manual for the Flexible DM-NRG code, [arXiv:0809.3143](https://arxiv.org/abs/0809.3143) (2008) (unpublished).
- [69] A. Weichselbaum and J. von Delft, Sum-Rule Conserving Spectral Functions from the Numerical Renormalization Group, *Phys. Rev. Lett.* **99**, 076402 (2007).
- [70] A. Weichselbaum, Tensor networks and the numerical renormalization group, *Phys. Rev. B* **86**, 245124 (2012).
- [71] T. A. Costi, Renormalization-group approach to nonequilibrium green functions in correlated impurity systems, *Phys. Rev. B* **55**, 3003 (1997).
- [72] A. I. Tóth, C. P. Moca, Ö. Legeza, and G. Zaránd, Density matrix numerical renormalization group for non-Abelian symmetries, *Phys. Rev. B* **78**, 245109 (2008).
- [73] A. Weichselbaum, F. Verstraete, U. Schollwöck, J. I. Cirac, and J. von Delft, Variational matrix-product-state approach to quantum impurity models, *Phys. Rev. B* **80**, 165117 (2009).
- [74] U. Schollwöck, The density-matrix renormalization group in the age of matrix product states, *Ann. Phys.* **326**, 96 (2011), January 2011 Special Issue.
- [75] M. Yoshida, M. A. Whitaker, and L. N. Oliveira, Renormalization-group calculation of excitation properties for impurity models, *Phys. Rev. B* **41**, 9403 (1990).
- [76] A. Rosch, Wilson chains are not thermal reservoirs, *Eur. Phys. J. B* **85**, 6 (2012).